

High-resolution three-dimensional imaging of the rich membrane structures of bone marrow-derived mast cells

T. Zink^a, Z. Deng^b, H. Chen^c, L. Yu^c, F.T. Liu^c, G.Y. Liu^{a,b,*}

^a Biophysics Graduate Group, University of California, Davis, CA 95616, USA

^b Department of Chemistry, University of California, Davis, CA 95616, USA

^c Department of Dermatology, School of Medicine, University of California-Davis, Sacramento, CA 95817, USA

ARTICLE INFO

Article history:

Received 7 September 2007

Received in revised form

1 May 2008

Accepted 23 July 2008

PACS:

68.37 Ps

87.64 Dz

Keywords:

Bone marrow-derived mast cells

Atomic force microscopy

Cell membrane

Ridges

Villi

Craters

High-resolution imaging

ABSTRACT

Atomic force microscopy (AFM) enables high-resolution three-dimensional (3D) imaging of cultured bone marrow-derived mast cells. Cells were immobilized by a quick centrifugation and fixation to preserve their transient cellular morphologies followed by AFM characterization in buffer. This “fix-and-look” approach preserves the structural integrity of individual cells. Well-known membrane morphologies, such as ridges and microvilli, are visualized, consistent with prior electron microscopy observations. Additional information including the 3D measurements of these characteristic features are attained from AFM topographs. Filopodia and lamellopodia, associated with cell spreading, were captured and visualized in three dimensions. New morphologies are also revealed, such as high-density ridges and micro-craters. This investigation demonstrates that the “fix-and-look” approach followed by AFM imaging provides an effective means to characterize the membrane structure of hydrated cells with high resolution. The quantitative imaging and measurements pave the way for systematic correlation of membrane structural features with the biological status of individual cells.

© 2008 Elsevier B.V. All rights reserved.

1. Introduction

Mast cells represent a class of key immunologic cells involved in immediate-type hypersensitivity [1,2]. They also play an important role in innate immunity [3,4] and in the pathogenesis of various diseases, especially allergy [5]. Bone marrow-derived mast cells (BMMCs) represent a key type of primary cells for the investigation of membrane structures in correlation with the hypersensitivity reactions or activation/allergy [6–9]. BMMCs exhibit dramatic changes in membrane morphology upon activation [10,11]. Some characteristic membrane morphologies in association with the activation status of mast cells were revealed

Abbreviations: 3D, three-dimensional; AFM, atomic force microscopy; BMMC, bone marrow-derived mast cell; DNP-BSA, dinitrophenol conjugated to bovine serum albumin; IgE, immunoglobulin E; FcεRI, high-affinity IgE receptor; FWHM, full-width-half-maximum; IL-3, interleukin-3; PBS, phosphate buffered saline solution; RBL, rat basophilic leukemia; RT, room temperature; SEM, scanning electron microscopy; TEM, transmission electron microscopy; CFSE, carboxy-fluorescein diacetate, succinimidyl ester

* Corresponding author at: Biophysics Graduate Group, University of California, Davis, CA 95616, USA. Tel.: +1 530 754 9678; fax: +1 530 754 8557.

E-mail address: liu@chem.ucdavis.edu (G.Y. Liu).

by previous studies involving microscopy [10–12], flow cytometry [13], liquid scintillation counts of radioactive labeled constituents [14], and sodium dodecyl sulfate-polyacrylamide gel electrophoresis [11,15].

Nanometer- to micron-sized membrane structures are characteristic of the cell's biological status. For example, it is postulated that functional signaling complexes may reside within membrane rafts [12,16,17], whose sizes are typically less than 100 nm [18–20]. In BMMCs, the signaling complexes [21,22] are initiated by receptor-mediated interactions(s) with the extracellular matrix [23] or solution environment. Electron microscopy (EM) studies [24,25] have attempted to capture these domains, containing the functional signaling complexes, by exposing the cytoplasmic membrane interface. Caveolae were identified as the site on the membrane where endocytosis and exocytosis occur [26–30]. Larger membrane features, such as villi and ridges, were viewed as a morphological indication of mast cell activation [10,11]. Filopodia and lamellopodia are associated with cell spreading or locomotion [31].

Despite variations found in different cell types and cell lines, previous scanning electron microscopy (SEM), transmission electron microscopy (TEM), and optical microscopy studies have

captured the following common and characteristic morphologies. EM studies indicate the general spherical cellular shape [32], implicit larger physical volume [11], and the presence of microvilli [10] as an indication of a quiescent mast cell. In contrast, the activated cellular morphology has been described as having a highly folded topography [10,33], often accompanied by cell spreading [10,11], ruffling in the periphery, and a smooth homogenous local apparent membrane texture on the cell surface [10,11,34]. While EM has proven to be a very informative technology in cellular structure characterization, some limitations have been identified [35]. All cells are dehydrated and imaged under vacuum. The membrane integrity and membrane fine structures may be compromised in the preparation processes [35]. In addition, EM characterization lacks 3D information that is important for quantizing and correlating various structural features with cellular signaling processes.

Originally founded by Binnig et al. [36] for molecular resolution of surface structures, AFM offers a high-resolution and membrane structural characterization, which is complementary to EM. AFM enables imaging in buffer or culture media; thus hydrated and living cells may be studied, and provides high-resolution 3D information [37]. The high-resolution live-cell imaging by AFM is still difficult to carry out as of today due to the soft-and-sticky interactions between the AFM probe and the cellular membrane surface, and the dynamic nature of the cellular membrane. Imaging fixed cells should prove to be informative upon faithful preservation of the structure of living cells [35]. AFM images of fixed and dehydrated cell samples have already suggested morphological information on rat basophilic leukemia (RBL) cells are similar to that provided by EM, e.g. a generally spherical cellular shape [38,39] implied larger volume [39], and the presence of a few fine filopodia [38,39] in non-activated cells and a highly folded topography with increased cell spreading in activated cells [38,39]. AFM imaging of live RBL cells was attempted and structural features were revealed [40]. This initial study [40] of hydrated cells demonstrates the potential of AFM in structural cellular biology. However, imaging primary cells of BMMCs still remains a challenge. This is partly due to the non-adherent nature of BMMCs and more complex protocols involved in attaining primary cells.

This work represents our initial effort in high-resolution AFM imaging of BMMCs. A “fix-and-look” method was utilized to assure the structural fidelity of cells and to circumvent the dynamic nature of the membrane. A state-of-the-art AFM was employed to attain high-resolution images of individual cells in phosphate buffered saline solutions (PBS). This investigation yields a systematic and comprehensive 3D high-resolution AFM imaging of BMMCs in their resting state, as well as under designed perturbations, i.e. dye uptake, immobilization on coated surfaces, and activation protocols. Characteristic structural features of villi and ridges, analogous to those found on RBL cells [10,23], were revealed. Locomotion structures, filopodia and lamellopodia, were captured with high resolution. Nano- and micro-sized features were measured in three dimensions. This work demonstrates the capability and high resolution of AFM in cell structural characterization, which lays the foundation for molecular-level imaging of living cells in correlation with signaling processes.

2. Materials and methods

2.1. Culture of BMMCs

The animal study was approved by the Institutional Animal Care and Use Committee of University of California, Davis. Bone marrow cells were collected from the femurs of C57BL6 mice and

cultured for 4–10 weeks in RPMI 1640 (Gibco) containing L-glutamine, 10% fetal bovine serum, and 20% conditioned medium from interleukin-3 (IL-3) producing cell line WEHI-3B, following established protocols [41,42]. The purity of mast cells exceeded 95%, as determined by the expression of FcεRI on the cell surface [43].

2.2. Coating of glass coverslips

BMMCs were immobilized on three specific surfaces, i.e. bare coverslips, poly-L-lysine (MW 1500–8000, 152689; MP Biomedicals)-coated, and DNP₃₀-BSA (dinitrophenol conjugated to bovine serum albumin; A23018; Invitrogen)-coated coverslips. Glass coverslips (Fisher Scientific) were rinsed three times with ultrapure water (18.2 MΩ cm; Milli-Q) followed by three rinses with PBS (137 mM NaCl, 2.7 mM KCl, 10 nM phosphate, pH 7.3–7.45; EM Science). For the coating with poly-L-lysine, the coverslips were then exposed to a PBS solution containing 1 mg/mL poly-L-lysine. For the coating of DNP₃₀-BSA, all coated coverslips were placed on a droplet of 200 μL containing 20 μg/mL of DNP₃₀-BSA and then incubated for 30 min at 37 °C. Later, the coverslips were rinsed and placed in a sterile 24-well culture plate (Nunc; Fisher Scientific) and kept moist with 0.5 mL of PBS.

2.3. Immobilization and fixation of BMMCs via a “fix-and-look” method

For this investigation, a “fix-and-look” approach was utilized to preserve the structural fidelity of the cells and to circumvent the fast structural changes due to membrane dynamics. Three precautions were taken prior to AFM imaging. First, serum-depleted media replaced the culture media for washing before immobilization to avoid serum attaching to the surface and to the cellular membrane. Second, short centrifugation time and immediate fixation were practiced to prevent structural degradation due to designed treatment procedures. Finally, trypan blue exclusion assays were performed on parallel samples to check the viability of the cells. Duplicate samples were stained with 10 μL of 4% trypan blue solution (Fluka; Sigma) as an indicator of cell viability. Trypan blue exclusion is a structural assay to test the viability of cells prior to fixation, which reveals only <2% death (blue cells) under our sample preparation conditions [44].

In stained cells, a cell cytosol dye, 5-(and 6) carboxyfluorescein diacetate, succinimidyl ester (CFSE; C1157, Ex. 490 nm, Em. 525 nm; Molecular Probes, Inc.) was used. CFSE indicates the cell's biological status, e.g. activation by the appearance of cavities devoid of dye, as well as increases of cell spreading behavior upon placing cells on a glass slide. Staining used 10 μg/mL of CFSE and 30 min incubation at 37 °C. Our laser scanning confocal microscopy [45] indicates that 98% of the cells remained viable (fluorescent without intracellular cavity) after centrifugation onto surfaces prior to fixation. This is consistent with the fact that CFSE is commonly used as a cell-tracing dye, and is considered little cytotoxicity to cells.

Sensitization of BMMCs involved the incubation of 5×10^5 cells/mL overnight with mouse anti-dinitrophenyl (DNP) IgE [46] at a concentration of 0.5 or 1 μg/mL. Later, both sensitized and control BMMCs were washed twice with PBS and then maintained in serum-free RPMI 1640 medium for 30 min to prevent serum attachment to the membrane. All solutions used were bath-warmed to 37 °C. Cells (5×10^5 cells/mL) were then centrifuged onto various coated glass coverslips at 320g on Marathon3000R (Thermoelectronic model 120; Fisher Scientific) for 5 min at 19–22 °C to obtain strong adhesion of cells to the surface.

Table 1
Summary of cell treatment conditions reported in this work

Figure index	IgE sensitization	Solution DNP-BSA	CFSE	Post-treatment incubation (min)	Poly-L-lysine	DNP-BSA
1A ₁	+	–	–	0	–	+
4A, 4B, 4C	–	–	+	30	–	–
1A ₂ , 1E ₁ , 1E ₂	n/a	n/a	n/a	n/a	n/a	n/a
1A ₃ , 5A	–	–	–	30	+	–
1B ₂	–	–	–	0	–	–
1B ₁ , 3A, 3B	–	–	–	30	–	–
3J	–	–	+	30	+	–
1B ₃ , 1C ₃ , 1D ₁ , 1D ₂ , 3C, 3D, 3K, 3L	+	–	–	30	–	+
1C, 3E	+	+	–	30	–	–
3F	+	+	–	30	+	–
3I	+	+	+	30	–	–
1C ₂ , 1D ₃	+	–	+	30	–	+
3H	–	+	+	30	+	–
1E ₃	–	+	–	30	+	–
2A	+	–	+	30	–	+

It is indicated that if the cells are sensitized with IgE, pre-exposed to growth dye (CFSE), the glass slides surfaces were coated with poly-L-lysine or DNP-BSA, or activated in solution via DNP-BSA.

The cells were incubated for two time periods after treatment of 0 and 30 min. Later, the cells were then washed with PBS again and fixed using 3.7% formaldehyde solution (Fisher) for 30 min at room temperature (RT). The fixed BMMCs were then stored in PBS, sealed with parafilms, and chilled on ice until imaging.

2.4. Treatment of BMMCs to attain characteristic membrane structures

We introduced various treatments to the BMMCs to test the sensitivity and resolution of AFM towards the membrane structural changes. The treatment strategies were based on two known facts: (a) mast cells can be activated by IgE cross-linkage using solution or surface-bound antigen molecules such as DNP₃₀-BSA; (b) BMMCs may be stimulated by polycations such as poly-L-lysine [18,23,46]. Specific cell treatment conditions are summarized in Table 1. Three examples follow to guide one's reading of Table 1. In Fig. 1A, the cell was sensitized overnight, rinsed, and spun onto a glass coverslip coated with DNP₃₀-BSA. The cell in Fig. 4A illustrated the dual roles of CFSE: to enhance cell spreading as well as to indicate cell viability. The cell in Fig. 3E represents a BMMC activated by antigen presented in solution. Procedures are as follows: sensitized cells were spun onto coverslips and then activated by the addition of DNP₃₀-BSA into the culture media to reach the final concentration of 100 ng/mL.

2.5. High-resolution AFM imaging and data analysis

An atomic force microscope (AFM; MFP3D; Asylum Research Inc., Santa Barbara, California, USA) combined with a laser scanning confocal microscope (Fluoview 1000; Olympus America Corp., USA) were used for structural characterization of the cell samples. The confocal microscope simultaneously collects three channels, and the fourth bright-field image is generated from the transmitted light detector. This optical synchronization enabled the precise placement and control of the AFM probes on a designated position on the cellular membrane. In addition, bright-field imaging was performed on samples stained with non-fluorescent trypan blue (cell viability assay), and confocal imaging was acquired for cells stained with fluorescent CFSE (cell-tracing dye) to check the viability for a specific treatment or perturbation prior to fixation.

The AFM scanner covers a range of $90 \times 90 \mu\text{m}^2$ in the XY plane and $16 \mu\text{m}$ in the Z-direction. Hydrated cells were imaged at RT in

PBS. Whole-cell images (Figs. 1 and 2) of the fixed specimens were conducted in the contact mode with a Si-based cantilever ($k = 0.03 \text{ N/m}$, CSC38 lever B; MikroMasch, USA). The multi-channel images of height, z-sensor, deflection, and lateral data were acquired. For higher resolution (or zoom-in view) at the nanoscopic scale, as seen in images displayed in Figs. 3 and 4, a Si_3N_4 ($k = 0.027 \text{ N/m}$, Olympus Biolever, lever B; Asylum Research Inc., USA) was used in the tapping mode. The tapping mode driving frequency ranges from 6 to 8 kHz. Imaging forces were typically less than 1 nN, as determined from force–distance curves after the experiments. The typical scan speed is from 0.3 to 1.0 Hz, with 512×512 pixels per frame.

Data display and analysis were compiled using MFP3D's software package written on Igor Pro platform (Wavemetrics). Measurements of selected features were obtained on unprocessed images. Two-dimensional quantification of cell circumference, contact area, and cell diameter measurements were done with ImageJ (NIH, version 1.36b) via a freehand selection tool in conjunction with a writing stylus. This combination provides truthful tracing of the irregular cell edge, as well as good reproducibility (less than 2% uncertainty). Cellular surface area upon immobilization was calculated from AFM topograph, using the masking methods available in the MFP3D software.

3. Results

3.1. Three-dimensional inspection of the overall morphology of individual BMMCs

The AFM imaging investigation enables visualization of individual cell morphology, as well as of mesoscopic features within each cell. This multi-dimensional visualization of membrane morphology allows the categorization of cells. Fig. 1 summarizes 12 characteristic morphologies from 1211 cells inspected under conditions specified in Table 1. Two criteria were considered in categorization of the BMMCs: (a) cell spreading behavior; and (b) membrane mesoscopic structures. In terms of membrane mesoscopic morphology, smooth membrane surface (Figs. 1A₁–A₃), and the presence of microvilli (Figs. 1B₁–B₃) and ridges (Figs. 1C₁–C₃, Figs. 1D₁–D₃, and Figs. 1E₁–E₃) were revealed. Upon activation of BMMCs, morphological changes are often accompanied by cell spreading [11], such as in Figs. 1A₂–E₃. Similar coupling behavior was also reported using AFM for dehydrated RBL cells after antigen activation [38,39,47]. Out of

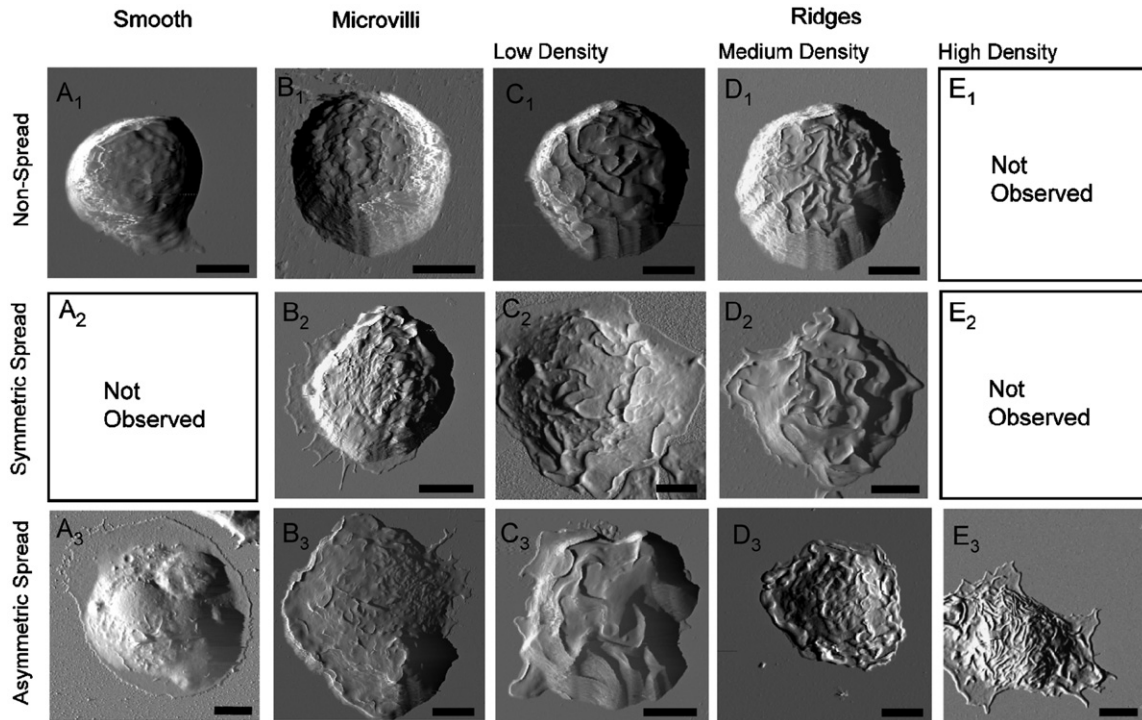


Fig. 1. AFM deflection images represent the 12 characteristic morphologies associated with cell spreading behavior. Escalating membrane texture (from left to right) can be observed in both symmetric (top rows, ratio < 1.2) and asymmetric BMMC morphology (bottom rows, ratio > 1.2). The corresponding quantification of cell spreading associated with these cells is provided in Table 1. Whole-cell images of the fixed specimens were conducted in the contact mode with CSC38 cantilevers ($k = 0.03$ N/m, lever B; MikroMasch). Scale bars are equal to $5 \mu\text{m}$.

Table 2

Quantitative characterization of cell spreading as represented by max/min diameters, interfacial circumference, and surface area at contact measurements were taken from AFM topographic images without image processing

Figure index	Diameter (μm) min/max	Ratio $D_{\text{max}}/D_{\text{min}}$	Maximum height (μm)	Circumference (μm)	Surface area at contact ($10^2 \mu\text{m}^2$)
1A ₁	13.0/15.4	1.19	8.99	43.05	2.58
1A ₃	23.2/29.7	1.28	3.80	129.62	4.95
1B ₁ , 3A	9.8/10.4	1.06	7.03	35.47	1.48
1B ₂ , 3B	13.3/14.2	1.06	7.18	56.97	2.35
1B ₃ , 3C	22.1/24.7	1.11	8.69	90.58	4.94
1C ₁ , 3E	14.5/14.6	1.00	9.68	49.05	2.77
1C ₂	21.6/23.0	1.08	6.23	86.44	4.29
1C ₃	15.0/20.4	1.35	9.82	74.48	4.07
1D ₁	15.9/16.0	1.01	10.71	53.50	3.74
1D ₂	16.2/18.3	1.12	6.58	69.68	3.65
1D ₃ , 3D, 4D	17.0/19.7	1.15	3.76	64.91	3.25
1E ₃	17.6/28.0	1.59	4.18	96.01	4.22

the 12 characteristic morphologies identified, two of them, the smooth non-spreading cell morphology (Fig. 1A₁) and the high ridge density morphology (Fig. 1E₃), have not been reported previously for mast cells.

The clearly resolved cell boundaries and 3D topography acquired by AFM, shown in Fig. 1, also enable the quantification of cell spreading and symmetry. Cell spreading is quantified by surface area, circumference, and cell height measured at the tallest point. The measurements are summarized in Table 2 for all 12 characteristic morphologies. Spreading behavior is defined by a surface projection greater than $180 \mu\text{m}^2$ area and a reduced cell height. A majority of treated cells, 90% ($n = 1090$), exhibited increased spreading in comparison to untreated and resting cells ($n = 121$). Overall cell height decreases by $\sim 20\%$ upon activation treatment in comparison to control cells on bare glass surfaces. Incubation time and the protocol of cell stimulation impacted the

detailed morphology of cell spreading. For example, within 10-min exposure to DNP-BSA, a complete loss of microvilli and transition to ridges were observed in cells. After 30 min, the overall cell height decreased from 5 to $3 \mu\text{m}$. In contrast, poly-L-lysine treatment resulted in spread cells with smooth membrane morphology and craters. The spreading cells were qualified or classified as asymmetric (ratio > 1.2) or symmetric (ratio < 1.2) based on the two extreme diameters and the diameter ratio, i.e. longest versus the shortest diameters at the interface.

Our systematic investigation (shown in Fig. 1 and Table 2) also revealed the coupling of characteristic structural features with cell spreading. Resting or non-activated cells typically exhibited a microvilli morphology without cell spreading (Fig. 1B₂). Ridges were observed in spreading cells in both symmetric (top two rows) and asymmetric morphology (bottom row) in Fig. 1.

Cell spreading and ridge density seem to correlate with ridge height, i.e. spreading cells with a high ridge density exhibited shorter ridges, typically $1\ \mu\text{m}$ less than those of the non-spreading cells with the same ridge density. Cells stained with CFSE tended to spread more than the non-stained counterparts. This exercise of structural classification provides a good basis for further systematic investigations to correlate cells' structure with their biological status, such as cell activation and migration.

3.2. Capturing transient structures associated with cell spreading or locomotion in a cell

Transient structure of a cell during movement was captured via fixation and is shown in Fig. 2. The AFM topography (Fig. 2A) and the corresponding deflection (Fig. 2B) images are displayed side-by-side. The AFM deflection image (Fig. 2B) allows a wide range of feature heights to be clearly visualized, because a large dynamic range ($10\ \text{nm}$ to $5\ \mu\text{m}$) is difficult to display linearly in the AFM topograph. The AFM topography on the other hand, provides the heights of the local structures of cell membrane in the 2D display (Fig. 2A) and 3D rendering (Fig. 2D). Detailed topography of structural features associated with single fixed cell was quantified using a series of cursor profiles taken across the

designated structures. Fig. 2C represents eight height measurements, as illustrated with the sagittal cursor plots. The 11 fine short protrusions at the leading edge had an approximate length range of $0.1\text{--}1\ \mu\text{m}$ and a maximum height of $0.5\ \mu\text{m}$, as obtained from the cursor plot number 6 and 7 in Fig. 2. One large tailing filopodium contains five branches. The main branch is $9.0 \pm 0.5\ \mu\text{m}$ long and with a maximum height of $1.10 \pm 0.06\ \mu\text{m}$ as displayed in the cursor profile (Fig. 2C₈). The large pseudopodia have been reported via EM in BMMCs [11,48]. Four regressing side branches ranged from 1 to $5\ \mu\text{m}$ in length.

First, the 11 filopodia were observed in AFM deflection and topograph images in Fig. 2 are characteristic of cell movement and spreading, as per previous reports [31,49]. Time-lapse differential interference contrast (DIC) microscopy investigations [50,51] in fibroblasts and Swiss 3T3 cells identified filopodia as being specific to cell movement and spreading. In addition, multiple small podia typically represent the leading edge of cell spreading [50–52], while a large tail or tails correspond to the trailing edge [50]. With the podia features clearly visualized and quantified in Fig. 2, the direction of locomotion of this cell, prior to fixation, can then be extracted. Therefore, based on the literature [31,47–50], the cell in Fig. 2A was moving from the top to the bottom before fixation. We can estimate the center of mass by integration of the

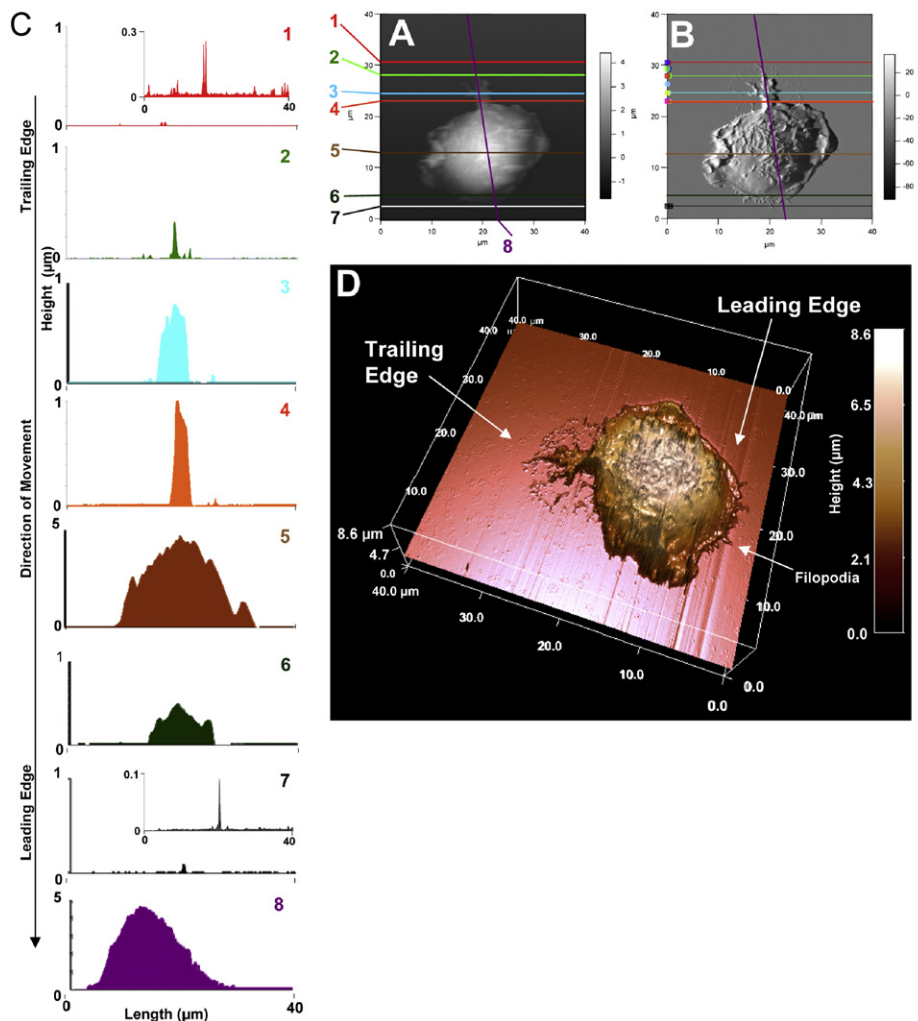


Fig. 2. Membrane features associated with cell movement such as filopodia, and fine structures in the leading and trailing edges. (A) and (B) represent AFM topographies and the corresponding deflection images, respectively. BMMCs were stained with CFSE, sensitized overnight with anti-DNP-IgE and then spun onto a glass coverslip coated with DNP-BSA. After 30 min incubation, cells were fixed with 3.7% formaldehyde for 30 min. (C) is a 3D rendering of the topographic image. Cursor profiles crossing the filopodia shown in (A) and (B) are shown in the left column to provide corresponding height data at a given cursor line. AFM images of the fixed cell was conducted in the contact mode with CSC38 cantilevers ($k = 0.03\ \text{N/m}$, lever B; MikroMasch).

sectioned areas (Figs. 1C₁–C₈) and from the overall cell shape (Fig. 2D), noticing the center of mass is closer to the leading edge, which is characterized by a lamellopodia associated with multiple small filopodia pointing to the direction of travel [49].

3.3. Three-dimensional quantification of characteristic membrane features including microvilli and ridges

Zooming into selected cells, rich membrane topographies were revealed by AFM imaging. The mesoscopic-scale images shown in Fig. 3 represent 12 characteristic membrane features acquired from 94 BMMCs images. The 12 images were distinguished by overall cell membrane morphology, as well as by the dimension and distribution of these characteristic features.

The most common structural feature of resting BMMCs, as observed by AFM and SEM [23,33,53], is microvilli or elevated domains, as shown in AFM images in Figs. 3A and B. These villi are visible from whole-cell images as shown in Figs. 1B₁–B₃, and are best resolved at higher resolution scans in Figs. 3A–C, from which 3D information can be extracted. For example, there were 39 villi in $5 \times 5 \mu\text{m}^2$ area with a maximum height of $0.47 \pm 0.05 \mu\text{m}$ and full-width-half-maximum (FWHM) of $0.3 \pm 0.1 \mu\text{m}$ for a typical microvilli membrane area as shown in Fig. 3A. Some of the BMMCs, upon challenge with DNP-BSA, present with villi structures as observed in Fig. 3C, with heights ranging from 0.27 to 1.19 μm .

The most well-known feature of activated BMMC is membrane ridges as seen by prior EM investigations mostly on RBL and some on BMMCs [10,11,33–34,39–42]. These features were readily captured in our AFM experiments. A majority of the activated

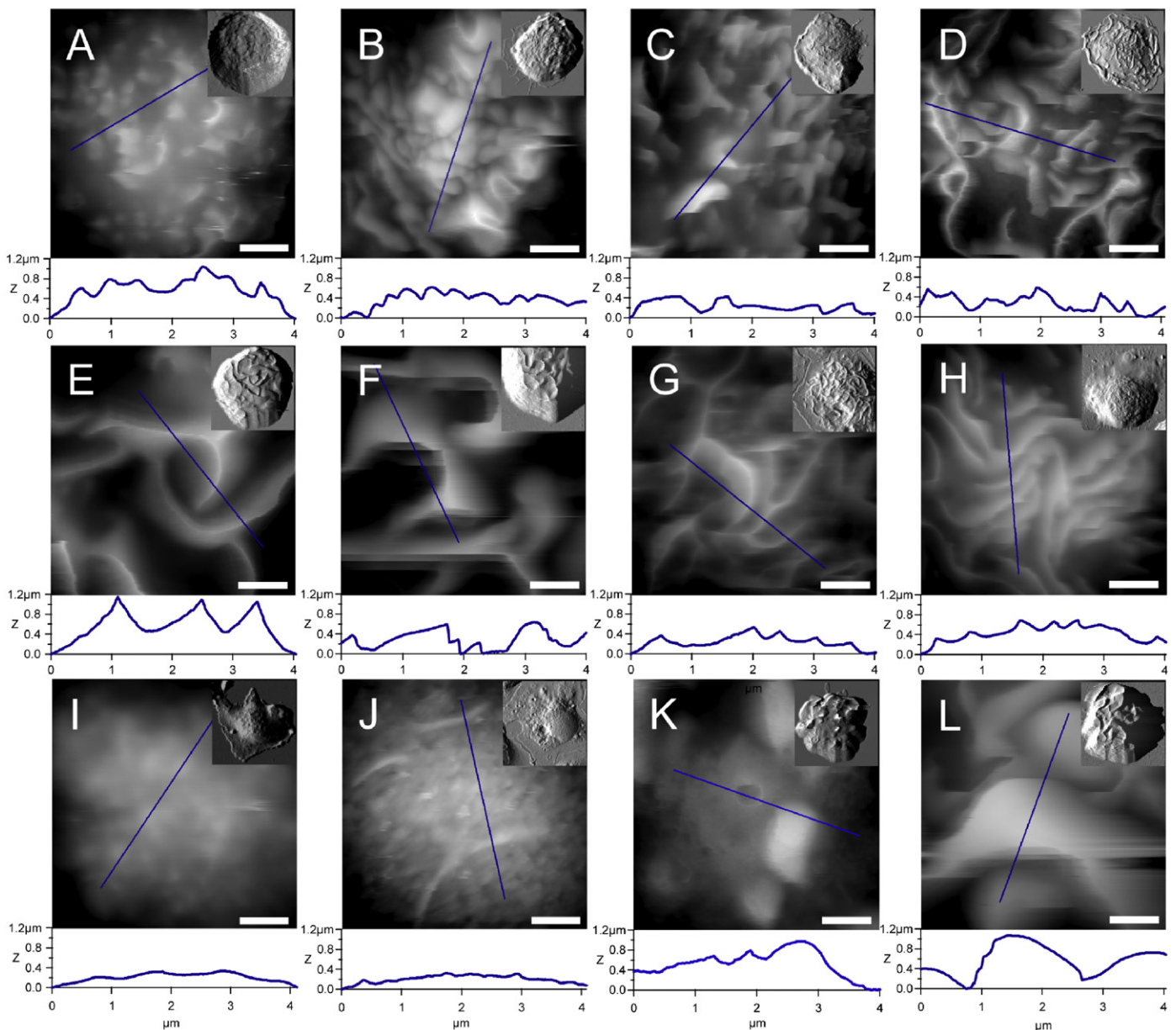


Fig. 3. Twelve characteristic mesoscopic structures of BMMC membranes are captured via AFM imaging. The quantitative measurements of local membrane fine structures may be extracted from extensive cursor profiles as exemplified underneath each image. Whole-cell images, in small box inset, were conducted in the contact mode with CSC38 cantilevers ($k = 0.03 \text{ N/m}$, lever B; MikroMasch). In order to achieve a higher resolution at the mesoscopic scale (large frames A–L), an Olympus Biolever ($k = 0.027 \text{ N/m}$, lever B) was used in the tapping mode. Scale bars are equal to 1 μm .

cells resulted in the appearance of ridges, with various sizes and densities. The 3D measurements revealed the ridge height ranging from 0.54 to 3.04 μm . The density of ridges was found to vary from 2 to 28 per 25 μm^2 scan area, by taking into account all spreading status as exemplified in Fig. 1. High density was referred to as greater than 20 ridges per 25 μm^2 membrane areas (e.g. Fig. 1E₃). The characteristic ridge features are shown in the middle row of Figs. 3D–H, where the total numbers (or density) increase from left to right. In Fig. 3E, the density can be described as five ridges in a $5 \times 5 \mu\text{m}^2$ area, with an FWHM value of $0.4 \pm 0.1 \mu\text{m}$ and ridge height of $1.21 \pm 0.01 \mu\text{m}$. A discrete maximum ridge height decreases with increasing ridge density. For example, one can compare a cell with high ridge density with a discrete ridge height of $0.21 \pm 0.01 \mu\text{m}$ in Fig. 3H to a cell with lower ridge density (Fig. 3F) and a taller discrete ridge height of $1.00 \pm 0.03 \mu\text{m}$.

Bulges are worm-like in shape as seen in Fig. 3K, with lateral dimension ranging from 0.20 to 0.64 μm and length ranging from

0.70 to 7.30 μm . In Fig. 3B, the bulges are closely packed and easily revealed. Figs. 3C and D may be envisioned as the transition of those bulges from dull (radius = $0.11 \pm 0.05 \mu\text{m}$ with a ridge length of $0.22 \pm 0.05 \mu\text{m}$) to sharp curvature (radius = $0.17 \pm 0.05 \mu\text{m}$ with a ridge length of $1.22 \pm 0.05 \mu\text{m}$). Figs. 3I and J display a smooth membrane morphology containing nanoscopic domains, not as elevated as Fig. 3A. These smooth areas are decorated occasionally by line-like protrusions as shown in Fig. 3J.

The fix-and-look approach enabled the capturing of a rare mixture of ridges, unusual discrete villi, and tall bulges ($>2 \mu\text{m}$) in some BMMCs upon antigen challenges, as shown in Figs. 3K and L, respectively. After careful comparison of the AFM data to the reported SEM morphologies [10,11,33,34,39–42], we note that Figs. 3B, L, and J represent new morphologies. The 3D and high-resolution morphological information not only confirmed the known structural features associated with mast cells' status, such as villi and ridges, but also enables quantification of the features.

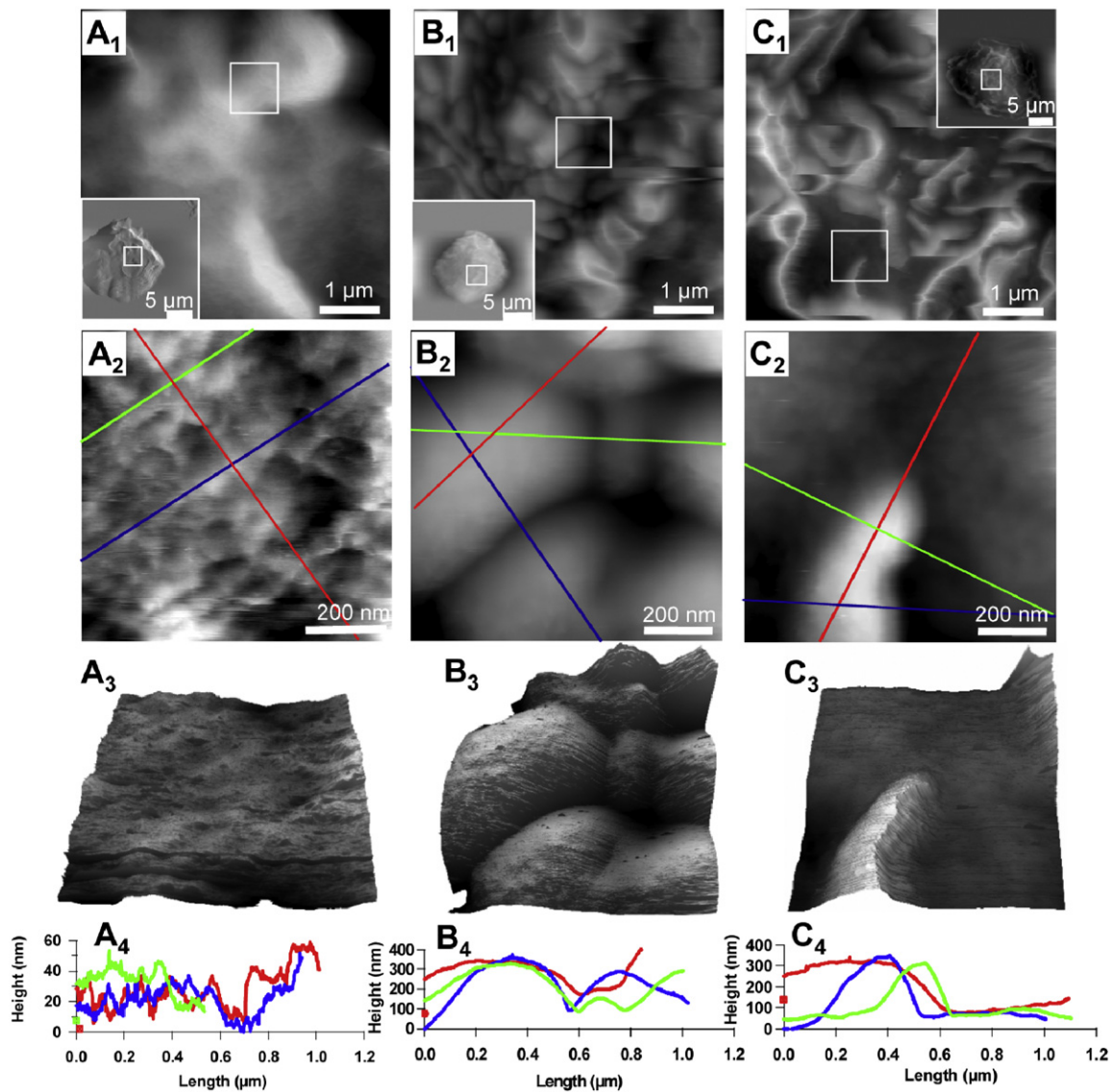


Fig. 4. Membrane fine structures at the nanometer scale as revealed by AFM. The large scans are shown as an inset in the first row, from which the systematic zoom-in images were acquired, as indicated by the white frames. AFM topographies displayed in the top row represent $5 \times 5 \mu\text{m}^2$ scan at the top of cell membrane (see inserts). Mesoscopic features, such as villi and ridges, are clearly visible at this scan. Further zoom onto individual features (see top row frames) enables nanoscopic features to be revealed, as shown in the second row. The third row is a 3D display of the nanoscopic feature, under which cursor profiles are provided to reveal the quantitative information. An Olympus Biolever ($k = 0.027 \text{ N/m}$, lever B) was used in the tapping mode for the nanoscopic frames (Figs. 4A₂–A₃, B₂–B₃, C₂–C₃).

3.4. Nanoscopic imaging of characteristic membrane features

The sample preparation methodology enabled fine and local structures of the cell membrane to be preserved at nanoscopic levels. Tapping-mode AFM was utilized to avoid the soft-and-sticky interactions between the probe and cellular surfaces [54]. The overall morphology of a chosen cell was surveyed using a large-area scan ($25 \times 25 \mu\text{m}^2$). Then, systematic zoom-in directs

the probe to specified regions, i.e. a $5 \times 5 \mu\text{m}^2$ and then $1 \times 1 \mu\text{m}^2$ area within the cell, to reveal the detailed structures at the nanoscale. Fig. 4 reveals characteristic features for this experiment. The high-resolution images are displayed in 2D (middle row) and in 3D (third row) for detailed visualization of the membrane's heterogeneity.

In the first column of Fig. 4, the cell membrane exhibits occasional large protrusions surrounded by smooth areas.

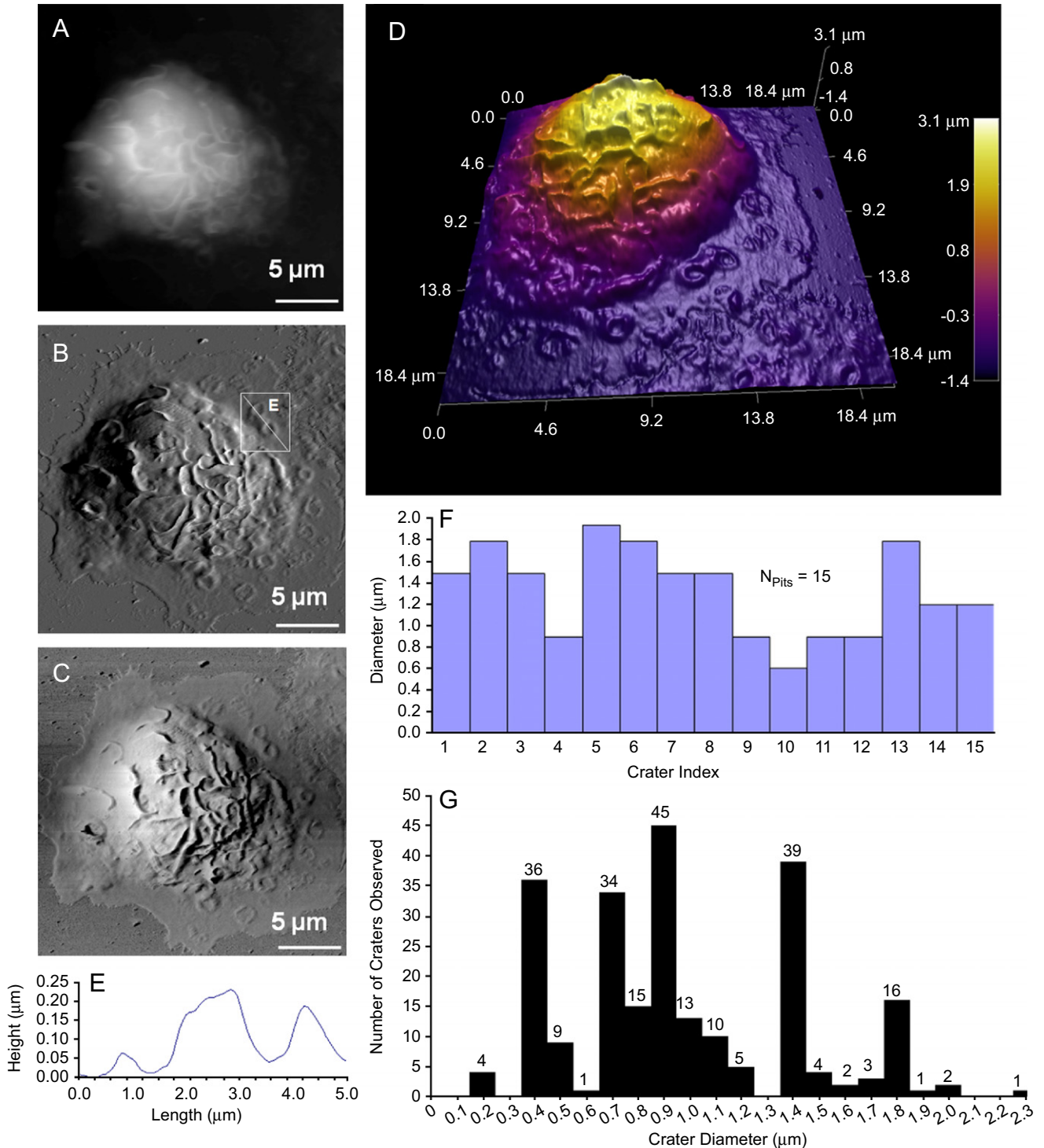


Fig. 5. Craters are observed at the membrane surface of BMMCs absorbed onto poly-L-lysine. (A), (B), and (C) represent the height, deflection, and lateral images of the chosen BMMC, respectively. A 3D rendering of the AFM topograph is provided in (D). The width and depth of craters can be measured from cursor profiles as illustrated in (E) and summarized in (F). Out of 37 cells presenting with 240 craters, the histogram displays the frequency of crater diameters in the graph (G). AFM images of the fixed cell were conducted in the contact mode with CSC38 cantilevers ($k = 0.03 \text{ N/m}$, lever B; MikroMasch).

The zoom-in image on Fig. 4A₂ reveals the relatively smooth portion of the membrane, while nano-sized features were clearly visible with 20 nm resolution. The topographic landscape is discernable in the 3D display (Fig. 4A₃) of Fig. 4A₂. The cursor profiles revealed that those nano-sized features were closely packed, with the diameter range of 40–200 nm and the height range of 1–30 nm (Fig. 4A₄).

Nanoscale features associated with transitional structure from microvilli to ridge formation were observed and are shown in Fig. 4. Subsequent zoom-in image of Fig. 4B₁ resulted in the resolution of clear boundaries at the interface of the round bulges. These local domains were more clearly visualized in the final zoom-in scan as shown in Fig. 4B₂, where ellipsoidal bulges are packed very tightly, as shown in 3D display (Fig. 4B₃). The dimensions of the bulges can be extracted from cursor profiles in Fig. 4B₄, where a small bulge measured 324 ± 30 nm along the long axis, 132 ± 30 nm along the short axis, and had an apparent height of 250 ± 30 nm. The largest bulge in Fig. 4B₂ measured 690 ± 30 nm length along the long-axis direction, 592 ± 30 nm along the short axis, and had an apparent height of 364 ± 30 nm.

More characteristic membrane structures associated with activation are the ridges or highly folded membrane placates as shown in the right column in Fig. 4. In contrast to the rounded protrusions, sharp ridges dominate the cells as shown in Fig. 4C. In Fig. 4C₁, there is a mixture of straight and curved lines, representing a total of 21 ridges in the $5 \times 5 \mu\text{m}^2$ scan area. From one characteristic ridge shown more clearly in the zoom-in image in Fig. 4C₂, the apparent maximum height of 372 ± 40 nm and FWHM of 311 ± 40 nm were obtained. Confirmed in both trace topograph and retrace topograph (data not shown) via the tapping mode AFM, the ridge as shown in Fig. 4C₂ is asymmetric and is reflected in the cursor profile (Fig. 4C₄) and is visualized in the 3D display in Fig. 4C₃.

3.5. Crater formation upon contact with poly-L-lysine-covered surfaces

Additional characteristic structural features captured in the AFM investigation are craters in the BMMC cell membranes. A specific example of the coexistence of ridges and craters is shown in Fig. 5, which contains 15 craters. This cell was stained with $5 \mu\text{M}$ of CFSE and centrifuged onto a glass coverslip coated with poly-L-lysine. Height, deflection, and lateral force images of a single cell were captured simultaneously in a $25 \times 25 \mu\text{m}^2$ scan. A maximum cell height of $4.10 \pm 0.03 \mu\text{m}$ was observed due to spreading, as regular BMMC exhibited a cell height of $6 \mu\text{m}$. The heterogeneity of the cell membrane containing ridges, domains, and craters are more clearly visible in Fig. 5D, where 3D rendering of the cell topography is provided. Each crater was quantified from the corresponding cursor profiles, as the example illustrated in Fig. 5E, where a selected cursor plot of two side-by-side features is seen. The two craters clearly visible in Fig. 5E exhibit a depth of 52 and 157 nm, respectively. The craters observed in this cell range from $2 \mu\text{m}$ down to $0.7 \mu\text{m}$ in inner diameter, and 51–193 nm in depth, as summarized in Fig. 5F.

Craters were observed only in viable cells exposed to poly-L-lysine-coated surfaces. Three separate experiments with two consecutive BMMC cultures consistently showed a 7% cell population ($n = 545$ cells) presenting with structures described as small semispherical craters. The craters were distributed throughout the cell surface, but had a higher frequency and were better resolved in the periphery where the cellular membrane flattening was maximized. The AFM images of 37 cells presenting 240 craters present a fairly uniform distribution of crater diameter sizes. The most frequent diameter size observed was $1.4 \mu\text{m}$ (45 out of 240 craters) with the second-most prevalent size value

of $0.9 \mu\text{m}$ (39 out of 240 craters). On average, there are six craters per cell, but up to 23 craters were seen in a single cell.

4. Discussion

The validity of AFM imaging of BMMCs is clearly demonstrated by visualization of well-known cell morphological features such as ridges, microvilli, lamellopodia, and filopodia, and by the finding of new features, such as craters and high-density ridges. The 3D and high resolution membrane structures enable correlation between the nano- and meso-scale membrane features with the cellular function or signaling processes. Cell locomotion has been associated with important biological processes, like cell colonization associated with metastasis [48,52,55]. For instance, the direction of cell migration and the consistency of the location of the center of mass (estimated from the 3D cell shape) enabled the determination of how a cell transports its mass during migration [47]. Morphological view and 3D quantification of structural features in Fig. 2, such as a filopodium and tails, provide important structural and geometrical information in accordance with cell locomotion.

The finding of craters on BMMCs exposed to poly-L-lysine indicates the exocytosis or discharging of granules that occurred upon immobilization and spreading. Based on the location and 3D size of these craters, we should be able to differentiate exocytosis from endocytosis. In endocytosis, membrane pores or caveolae are triggered by receptor-mediated activation, and typically this diameter is in the range 0.05 – $0.20 \mu\text{m}$ [10]. It was reported that large craters, 0.2 – $2.0 \mu\text{m}$, were associated with exocytosis [6,29–30,56]. Based on our most frequent diameter of $1.4 \mu\text{m}$ ($n = 37$) out of 240 craters observed, we conclude these craters are consistent with exocytosis.

We also excluded the possibility that these craters are due to poly-L-lysine-induced membrane damage, because the cell viability upon exposure to poly-L-lysine was demonstrated by previous studies [56]. Furthermore, in our CFSE labeling experiment (data not shown), there is no noticeable decrease in the overall fluorescence signal for the cells with craters, which will happen when the cell membrane is damaged. The sample heterogeneity is worth noting, i.e. only a portion of the BMMCs exhibits the craters, while some adjacent cells simultaneously imaged do not contain craters. The craters were observed in two different culture harvests with the only common factor of reproducibility on poly-L-lysine-coated coverslips. Craters have not been reported for BMMCs stimulated by IgE-crosslinker, such as DNP-BSA.

The similarity in morphology between SEM and AFM images mutually validates both techniques. Most of the EM sample treatments reveal visual similarities as AFM topographic images. AFM also provides additional 3D and high-resolution structural information on hydrated cells. This progress brings us closer to investigate more difficult problems in cellular biology; correlating characteristic membrane features with specific cell signaling processes. For example, function nano-sized membrane features (bulges and sharp tips at ridges) could be potentially linked with co-localization of receptors.

5. Conclusion

A systematic investigation using AFM is reported to reveal high-resolution 3D structural information of membrane morphology of the BMMCs. Mature and live cells were quickly immobilized, fixed, and imaged in PBS. This approach facilitated the capture of transient structures for visualization by AFM in their hydrated state. Well-known structural features, such as

ridges and microvilli, are revealed and quantified with 3D information. New morphologies and nanoscopic features are also revealed, which provided insight into how the mesoscopic features may correlate with the spreading and activation of BMMCs. Craters on the surface of the cell membrane were seen and characterized after exposing BMMCs to poly-L-lysine-coated surfaces. Lamellopodia and filopodia in individual cells were imaged with great detail and integrity, from which the movement directions were determined. The main advantages of this approach include the preservation of structural integrity, maintenance of the hydrated status, and high-resolution and quantitative 3D information of cells. Work is in progress to correlate this rich structural information with detailed status of cell signaling processes, such as activation. Future work will also target time-dependent studies on living cells during activation.

Acknowledgments

This work was supported by NIH (1R21 GM077850-01, R01AI20958, and R01AI39620) and UC Davis. Both T. Zink and Z. Deng are recipients of fellowships from Tyco Electronics Foundation in Functional Materials. We also thank Mr. Alan Hicklin at UC Davis' Spectral Imaging Facility and Dr. Deron Walters at Asylum Research Inc., for their technical assistance. We also thank all three reviewers for their constructive criticism, which improved the quality and clarity of this paper.

References

- [1] D.D. Metcalfe, D. Baram, Y.A. Mekori, *Physiol. Rev.* 77 (1997) 1033.
- [2] D. Carlos, A. Sa-Nunes, L. de Paula, C. Matias-Peres, M.C. Jamur, C. Oliver, M.F. Serra, M.A. Martins, L.H. Faccioli, *Eur. J. Immunol.* 36 (2006) 1494.
- [3] S.J. Galli, M. Maurer, C.S. Lantz, *Curr. Opin. Immunol.* 11 (1999) 53.
- [4] J.S. Marshall, D.M. Jawdat, *J. Allergy Clin. Immunol.* 114 (2004) 21.
- [5] L.B. Schwartz, *Curr. Opin. Immunol.* 6 (1994) 91.
- [6] T. Furuno, M. Nakanishi, *Biol. Pharm. Bull.* 28 (2005) 1551.
- [7] T. Fukao, T. Yamada, M. Tanabe, Y. Terauchi, T. Ota, T. Takayama, T. Asano, T. Takeuchi, T. Kadowaki, J. Hata, S. Koyasu, *Nat. Immunol.* 3 (2002) 295.
- [8] M.F. Gurish, J.A. Boyce, *J. Allergy Clin. Immunol.* 117 (2006) 1285.
- [9] S.J. Galli, J. Kalesnikoff, M.A. Grimbaldston, A.M. Piliponsky, C.M.M. Williams, M. Tsai, *Ann. Rev. Immunol.* 23 (2005) 749.
- [10] J.R. Pfeiffer, J. Seagrave, B.H. Davis, G.G. Deanin, J.M. Oliver, *J. Cell Biol.* 101 (1985) 2145.
- [11] Z. Xiang, M. Block, C. Lofman, G. Nilsson, *J. Allergy Clin. Immunol.* 108 (2001) 116.
- [12] A.M. Davey, R.P. Walvick, Y.X. Liu, A.A. Heikal, E.D. Sheets, *Biophys. J.* 92 (2007) 343.
- [13] D. Kaur, P. Berger, S.M. Duffy, C.E. Brightling, P. Bradding, *Clin. Exp. Allergy* 35 (2005) 226.
- [14] B.A. Faraj, G.R. Gottlieb, V.M. Camp, M. Kutner, P. Lories, *J. Nucl. Med.* 25 (1984) 56.
- [15] P.S. Jolly, M. Bektas, K.R. Watterson, H. Sankala, S.G. Payne, S. Milstien, S. Spiegel, *Blood* 105 (2005) 4736.
- [16] M. Wu, D. Holowka, H.G. Craighead, B. Baird, *Proc. Natl. Acad. Sci. USA* 101 (2004) 13798.
- [17] B. Grasberger, A.P. Minton, C. Delisi, H. Metzger, *Proc. Natl. Acad. Sci. USA* 83 (1986) 6258.
- [18] D.J. Frankel, J.R. Pfeiffer, Z. Surviladze, A.E. Johnson, J.M. Oliver, B.S. Wilson, A.R. Burns, *Biophys. J.* 90 (2006) 2404.
- [19] E.C. Lai, *J. Cell Biol.* 162 (2003) 365.
- [20] S. Munro, *Cell* 115 (2003) 377.
- [21] A.M. Gilfillan, C. Tkaczyk, *Nat. Rev. Immunol.* 6 (2006) 218.
- [22] M.A. Beaven, H. Metzger, *Immunol. Today* 14 (1993) 222.
- [23] J. Seagrave, J.R. Pfeiffer, C. Wofsy, J.M. Oliver, *J. Cell. Physiol.* 148 (1991) 139.
- [24] B.S. Wilson, J.R. Pfeiffer, J.M. Oliver, *Mol. Immunol.* 38 (2001) 1259.
- [25] C.M. Franz, D.J. Muller, *J. Cell Sci.* 118 (2005) 5315.
- [26] B.P. Jena, *J. Cell. Mol. Med.* 8 (2004) 1.
- [27] E. Crivellato, B. Nico, F. Mallardi, C.A. Beltrami, D. Ribatti, *Anat. Rec. A* 274A (2003) 778.
- [28] S. Kessler, C. Kuhn, *Lab. Invest.* 32 (1975) 71.
- [29] R. Nakamura, M. Nakanishi, *Immunol. Lett.* 72 (2000) 167.
- [30] S.W. Schneider, K.C. Sritharan, J.P. Geibel, H. Oberleithner, B.P. Jena, *Proc. Natl. Acad. Sci. USA* 94 (1997) 316.
- [31] T.P. Stossel, *Science* 260 (1993) 1086.
- [32] E. Razin, A. Cordoncardo, C.R. Minick, R.A. Good, *Exp. Hematol.* 10 (1982) 524.
- [33] M. Kurosawa, H. Inamura, N. Kanbe, Y. Igarashi, T. Tomita, J. Takeda, Y. Miyachi, *Clin. Exp. Allergy* 28 (1998) 1007.
- [34] A.J. Edgar, G.R. Davies, M.A. Anwar, J.P. Bennett, *Inflamm. Res.* 46 (1997) 354.
- [35] R.W.M. Hoetelmans, F.A. Prins, I. Cornelese-ten Velde, J. van der Meer, C.J.H. van de Velde, J.H. van Dierendonck, *Appl. Immunohistochem. Mol. Morphol.* 9 (2001) 346.
- [36] G. Binnig, C.F. Quate, C. Gerber, *Phys. Rev. Lett.* 56 (1986) 930.
- [37] J.M. Fernandez, *Proc. Natl. Acad. Sci. USA* 94 (1997) 9.
- [38] H. Ohshiro, R. Suzuki, T. Furuno, M. Nakanishi, *Immunol. Lett.* 74 (2000) 211.
- [39] R. Nakamura, M. Nakanishi, *Immunol. Lett.* 69 (1999) 307.
- [40] D. Braunstein, A. Spudich, *Biophys. J.* 66 (1994) 1717.
- [41] E. Razin, J.M. Menciahuerta, R.L. Stevens, R.A. Lewis, F.T. Liu, E.J. Corey, K.F. Austen, *J. Exp. Med.* 157 (1983) 189.
- [42] D. Hata, Y. Kawakami, N. Inagaki, C.S. Lantz, T. Kitamura, W.N. Khan, M. Maeda-Yamamoto, T. Miura, W. Han, S.E. Hartman, L. Yao, H. Nagai, A.E. Goldfeld, F.W. Alt, S.J. Galli, O.N. Witte, T. Kawakami, *J. Exp. Med.* 187 (1998) 1235.
- [43] H.Y. Chen, B.B. Sharma, L. Yu, R. Zuberi, I.C. Weng, Y. Kawakami, T. Kawakami, D.K. Hsu, F.T. Liu, *J. Immunol.* 177 (2006) 4991.
- [44] J.E. Coligan (Ed.), *Current Protocols in Immunology*, Greene Pub. Associates and Wiley-Interscience, New York, 1997 A.3B.1-A.3B.2pp.
- [45] Z. Deng, T. Zink, H.-Y. Chen, D. Walters, F.-T. Liu, G.-Y. Liu, The study of mast cell activation by a combination of atomic force microscopy, *Biophys. J.* (in preparation).
- [46] Z. Deng, T. Zink, H.-Y. Chen, D. Walters, F.-T. Liu, G.-Y. Liu, Impact of actin rearrangement and degranulation on the membrane structure of primary mast cells: a combined atomic force and laser scanning confocal microscopy investigation, *Biophys. J.*, submitted.
- [47] Z.Y. Liu, J.I. Young, E.L. Elson, *J. Cell Biol.* 105 (1987) 2933.
- [48] J. Kuchler, A. Grutzkau, B.M. Henz, S. Kruger-Krasagakis, *Arch. Dermatol. Res.* 298 (2006) 153.
- [49] J.P. Rieu, A. Upadhyaya, J.A. Glazier, N.B. Ouchi, Y. Sawada, *Biophys. J.* 79 (2000) 1903.
- [50] Y. Ohta, N. Suzuki, S. Nakamura, J.H. Hartwig, T.P. Stossel, *Proc. Natl. Acad. Sci. USA* 96 (1999) 2122.
- [51] T. Azuma, W. Witke, T.T. Stossel, J.H. Hartwig, D.J. Kwiatkowski, *EMBO J.* 17 (1998) 1362.
- [52] M.R. Mejillano, S. Kojima, D.A. Applewhite, F.B. Gertler, T.M. Svitkina, G.G. Borisy, *Cell* 118 (2004) 363.
- [53] N. Sahara, R.P. Siraganian, C. Oliver, *J. Histochem. Cytochem.* 38 (1990) 975.
- [54] C.A.J. Putman, K.O. Vanderwerf, B.G. Degrooth, N.F. Vanhulst, J. Greve, *Appl. Phys. Lett.* 64 (1994) 2454.
- [55] P. Mehlen, A. Puisieux, *Nat. Rev. Cancer* 6 (2006) 449.
- [56] N. Thiernesse, P. Jeannesson, J. Bernard, D. Zagury, G.A. Voisin, *J. Immunol. Methods* 21 (1978) 79.